

Physics-informed Neural Network for Acoustic Resonance Analysis in a One-Dimensional Acoustic Tube

Kazuya Yokota,^{1, a} Takahiko Kurahashi,¹ and Masajiro Abe²

¹*Department of Mechanical Engineering, Nagaoka University of Technology, Nagaoka, Niigata, 940-2188, Japan*

²*Department of System Safety Engineering, Nagaoka University of Technology*

This study devised a physics-informed neural network (PINN) framework to solve the wave equation for acoustic resonance analysis. The proposed analytical model, ResoNet, minimizes the loss function for periodic solutions and conventional PINN loss functions, thereby effectively using the function approximation capability of neural networks while performing resonance analysis. Additionally, it can be easily applied to inverse problems. The resonance in a one-dimensional acoustic tube, and the effectiveness of the proposed method was validated through the forward and inverse analyses of the wave equation with energy-loss terms. In the forward analysis, the applicability of PINN to the resonance problem was evaluated via comparison with the finite-difference method. The inverse analysis, which included identifying the energy loss term in the wave equation and design optimization of the acoustic tube, was performed with good accuracy.

[The following article has been submitted to the Journal of the Acoustical Society of America. After it is published, it will be found at <https://pubs.aip.org/asa/jasa>.]

[<https://doi.org/DOI number>]

[XYZ]

Pages: 1–15

I. INTRODUCTION

Machine learning has made significant advances over the last decade, yielding state-of-the-art methods in numerous fields including speech synthesis^{1,2} and image recognition^{3,4}. Advances in machine learning have enhanced numerical simulation technology, which has been applied to turbulence models^{5,6}, design optimization of machine materials⁷, and to accelerate the computation time in fluid analysis^{8,9}. Recent years have seen an increased demand for machine learning in numerical simulation as it effectively addresses inverse problems such as design optimization and parameter identification. The physics-informed neural network (PINN), proposed by Raissi et al.¹⁰, is a numerical analysis method that introduces constraints on the governing partial differential equations (PDEs) in the loss functions of a neural network. In PINN, a loss function based on PDE residuals evaluated by automatic differentiation (AD)¹¹ along with the loss functions of the initial and boundary conditions are defined and then minimized to obtain the simulation results. The PINN can be used for inverse problems to identify uncertain parameters of the governing PDEs. It has also been applied in thermodynamics and fluid mechanics for parameter identification of the equation of state¹², application to inverse problems in supersonic flows¹³, and identification of the thermal diffusivity of materials¹⁴.

Despite the aforementioned advances in PINN, their application in acoustics has been limited. Moreover, although the wave equation governing the acoustic phenomena is linear, it is subject to reflection, interference, and diffraction, and its solutions have a wide range of amplitudes and frequencies¹⁵. Therefore, the dynamics of sound waves can be extremely complex, hindering the development of PINN for acoustic analysis¹⁶. Few studies have analyzed acoustic resonance using PINN.

Existing studies that employed PINN for wave equation analyses^{16–18} have considered only unidirectional traveling waves or a small number of acoustic wave reflections and interferences. Thus, they do not apply to resonance phenomena. Several practical PINN based on the wave equation have been reported for seismic wave analysis^{19–21}; however, they are for large-scale Earth's ground and inapplicable to sound fields with complex dynamics, such as those of human-scale acoustic instruments. A previous study on acoustic holography using PINN based on the Kirchhoff–Helmholtz integral^{22,23} demonstrated the applicability of PINN to acoustic resonance; however, this resonance analysis was in the frequency domain and could not perform time-dependent analysis.

In this context, N. Borrel-Jensen et al. constructed PINN by introducing reflection boundary conditions and reported that PINN could analyze 1D acoustic resonance using actual physical conditions of air²⁴. They also reported 3D acoustic resonance analysis²⁵ using DeepONet²⁶ and showed that although it takes several

^ayokokazu@vos.nagaokaut.ac.jp

hours to learn, predictions can be made on the millisecond scale. These reports suggest the possibility of acoustic analysis using neural networks.

Time-domain analysis of resonance is critical in the field of acoustics. For example, the two-mass model^{27,28} and body-cover model^{29,30} describing vocal fold vibrations in speech production, describe vocal fold vibrations as equations in the time domain. The equations describing lip motion in brass instruments^{31,32} and reed motion in woodwinds^{33,34} are also described as time-domain equations. These coupled vibration-acoustic analyses often include time-dependent and nonlinear terms such as vocal collisions³⁵, which require time-domain simulations. Therefore, time-domain analysis of resonance using PINN could considerably benefit various acoustics fields. PINN can perform inverse analysis with the same neural network structure as forward analysis and can be used to identify uncertain parameters of the governing PDEs, as mentioned above. Therefore, PINN has the potential to greatly advance the field of inverse analysis in acoustics, such as the diagnosis of speech disorders known as Glottal Inverse Filtering (GIF)³⁶, the estimation of vocal tract shape³⁷ and design optimization of acoustic equipment.

In this study, we developed ResoNet, a PINN that analyzes acoustic resonance in the time domain based on the wave equation while effectively utilizing the function approximation capability of neural networks³⁸ by training the neural network to minimize the loss function with respect to periodic solutions. The main contributions of this study are as follows: (i) this study devised a periodicity loss function that effectively utilizes the function approximation capability of neural networks when using the PINN for analyzing 1D resonances in the time domain; (ii) it entailed a detailed investigation of the applicability of PINN to 1D acoustic resonance analysis; and (iii) it examined the performance of inverse problem analysis on 1D acoustic resonance phenomena.

The remainder of this paper is organized as follows. Section II describes the one-dimensional wave equation with energy loss terms and the acoustic field setup analyzed in this study. Section III describes ResoNet, a PINN that analyzes resonances based on the wave equation described in Section II. Section IV describes the forward and inverse analyses using ResoNet and its performance. Section V summarizes the study and discusses the application potential of PINN in acoustic resonance.

II. GOVERNING EQUATIONS OF ACOUSTIC RESONANCE

This section describes the wave equation and the acoustic field setup analyzed in this study.

A. One-dimensional wave equation with energy loss terms

We considered the propagation of plane sound waves in an acoustic tube of length l and circular cross-sectional area of $A(x)$, as shown in Fig. 1, with x as the axial

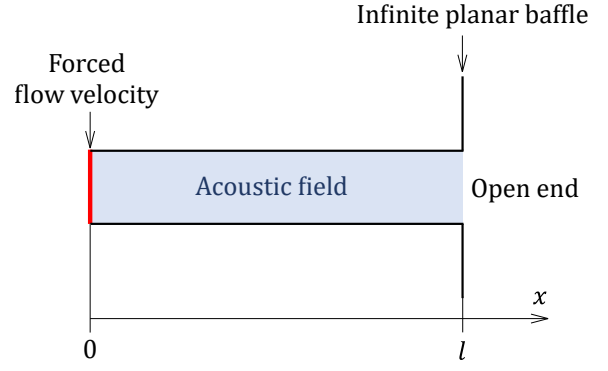


FIG. 1. (Color online) The 1D acoustic tube that is the subject of the analysis in this study. The flow boundary condition is given at the left end, and the right end is the open end. The radiation at the open end is modeled by the equivalent circuit shown in Fig. 2.

direction. Let the sound pressure in the acoustic tube be p and air volume velocity be u . Assuming $p = Pe^{j\omega t}$ and $u = Ue^{j\omega t}$, the telegrapher's equations for the acoustic tube considering energy loss are as follows³⁹.

$$\frac{dU}{dx} = - \left(G + j\omega \frac{A}{K} \right) P, \quad (1)$$

$$\frac{dP}{dx} = - \left(R + j\omega \frac{\rho}{A} \right) U, \quad (2)$$

where G is the coefficient of energy loss owing to thermal conduction at the tube wall; R is the coefficient of energy loss owing to viscous friction at the tube wall; j is the imaginary unit; ω is the angular velocity; K is the bulk modulus; and ρ is the air density. Equations (1) and (2) can be expressed in the time domain, as follows.

$$\frac{\partial u}{\partial x} = -Gp - \frac{A}{K} \frac{\partial p}{\partial t}, \quad (3)$$

$$\frac{\partial p}{\partial x} = -Ru - \frac{\rho}{A} \frac{\partial u}{\partial t}. \quad (4)$$

The velocity potential ϕ is defined as:

$$u = -A \frac{\partial \phi}{\partial x}, \quad (5)$$

$$p = RA\phi + \rho \frac{\partial \phi}{\partial t}. \quad (6)$$

Note that u is volume velocity. From equations (3)-(6), we obtain the following wave equation with energy loss terms, as follows.

$$\frac{\partial^2 \phi}{\partial x^2} + \frac{1}{A} \frac{\partial A}{\partial x} \frac{\partial \phi}{\partial x} = GR\phi + \left(\frac{G\rho}{A} + \frac{RA}{K} \right) \frac{\partial \phi}{\partial t} + \frac{\rho}{K} \frac{\partial^2 \phi}{\partial t^2}. \quad (7)$$

A detailed derivation of Eq. (7) is provided in Appendix A.

Theoretical solutions for R and G have been proposed, as follows, under the assumptions that the wall

surface is rigid and thermal conductivity is infinite³⁹.

$$R = \frac{S}{A^2} \sqrt{\frac{\omega_c \rho \mu}{2}}, \quad (8)$$

$$G = S \frac{\eta - 1}{\rho c^2} \sqrt{\frac{\lambda \omega_c}{2 c_p \rho}}, \quad (9)$$

where S is the circumference of the acoustic tube; μ , η , c , λ , and c_p are the viscosity coefficient, heat-capacity ratio, speed of sound, thermal conductivity, and specific heat at constant pressure, respectively; and ω_c is the angular velocity used to calculate the energy loss term. As R and G vary with the physical properties of air and the condition of the walls of the acoustic tube, these parameters are generally unknown. We confirmed that the energy loss parameters of the acoustic tube should be measured experimentally⁴⁰. Additionally, as demonstrated in vocal tract analysis, we have experimentally confirmed that the energy loss parameters can be approximated as frequency-independent constants in a limited frequency range⁴⁰. Therefore, in this study, ω_c was set as constant, and consequently, R and G were assumed to be frequency-independent constants.

B. Acoustic field and boundary conditions

The acoustic field analyzed in this study is shown in light blue in Fig. 1. The acoustic tube was straight, with a forced-flow boundary condition at $x = 0$. It had an open end with an infinite planar baffle at $x = l$, and the boundary condition was given by the equivalent circuit described in Section II C.

The aforementioned boundary conditions are fundamental in human speech production^{27,28} and in the acoustic analysis of brass instruments⁴¹. In this study, we used these boundary conditions to investigate the performance of resonance analysis with PINN.

C. Modeling of radiation

This section describes the modeling of the radiation at $x = l$ in Fig. 1. Assuming that the particle velocity at the open end is uniform, air at the open end can be regarded as a planar sound source. In response to the acoustic radiation, the plane receives sound pressure p_l from outside the acoustic tube. If an infinite planar baffle surrounds the open end, the relationship between volume velocity u_l at the open end and p_l can be approximated using the equivalent circuit shown in Fig. 2²⁷. In Fig. 2, the volume velocity u_l corresponds to the current and the sound pressure p_l to the voltage. The equations connecting u_l and p_l are as follows.

$$(u_l - u_r) R_r = L_r \frac{du_r}{dt}, \quad (10)$$

$$p_l = (u_l - u_r) R_r, \quad (11)$$

where R_r is the circuit resistance; L_r is the circuit reactance; and u_r is the current (corresponding to the volume

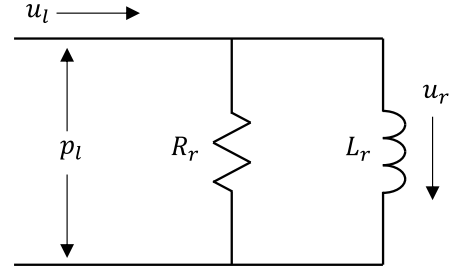


FIG. 2. Equivalent circuit of acoustic radiation. u_l is the volume velocity at $x = l$. The volume velocity corresponds to the current, and the pressure corresponds to the voltage.

velocity) flowing through the coil side. Here, R_r and L_r are expressed as follows.

$$R_r = \frac{128 \rho c}{9 \pi^2 A_l}, \quad (12)$$

$$L_r = \frac{8 \rho}{3 \pi \sqrt{\pi A_l}}, \quad (13)$$

where A_l denotes the cross-sectional area for $x = l$.

III. PROPOSED METHOD

This section describes the structure of ResoNet, a PINN for analyzing the acoustic resonance, and a training method for the neural network.

A. Overview of ResoNet

Fig. 3 shows the proposed neural network structure for the resonance analysis in acoustic tubes, referred to as ResoNet. As shown in Fig. 3, ResoNet has two blocks of neural networks.

The first is a network that calculates the solutions to the wave equation in Eq. (7), taking x_i and t_i as inputs (where i is the sample number) to predict the velocity potential $\hat{\phi}_i$. In this study, this input-output relationship is expressed using the following equation:

$$\hat{\phi}_i = F_w(x_i, t_i; \Theta_w), \quad (14)$$

where F_w is the operator of the neural network for the wave equation, and Θ_w is the set of trainable parameters of the neural network.

The other is a network for calculating the acoustic radiation, utilizing t_i as the input for predicting \hat{u}_{ri} by calculating the solution of the equivalent circuit in Fig. 2. The input-output relationship is expressed as:

$$\hat{u}_{ri} = F_r(t_i; \Theta_r), \quad (15)$$

where F_r is the neural network operator for acoustic radiation analysis, and Θ_r is the set of trainable neural network parameters.

The reason for using two neural networks instead of one with two outputs is to modify the neural network

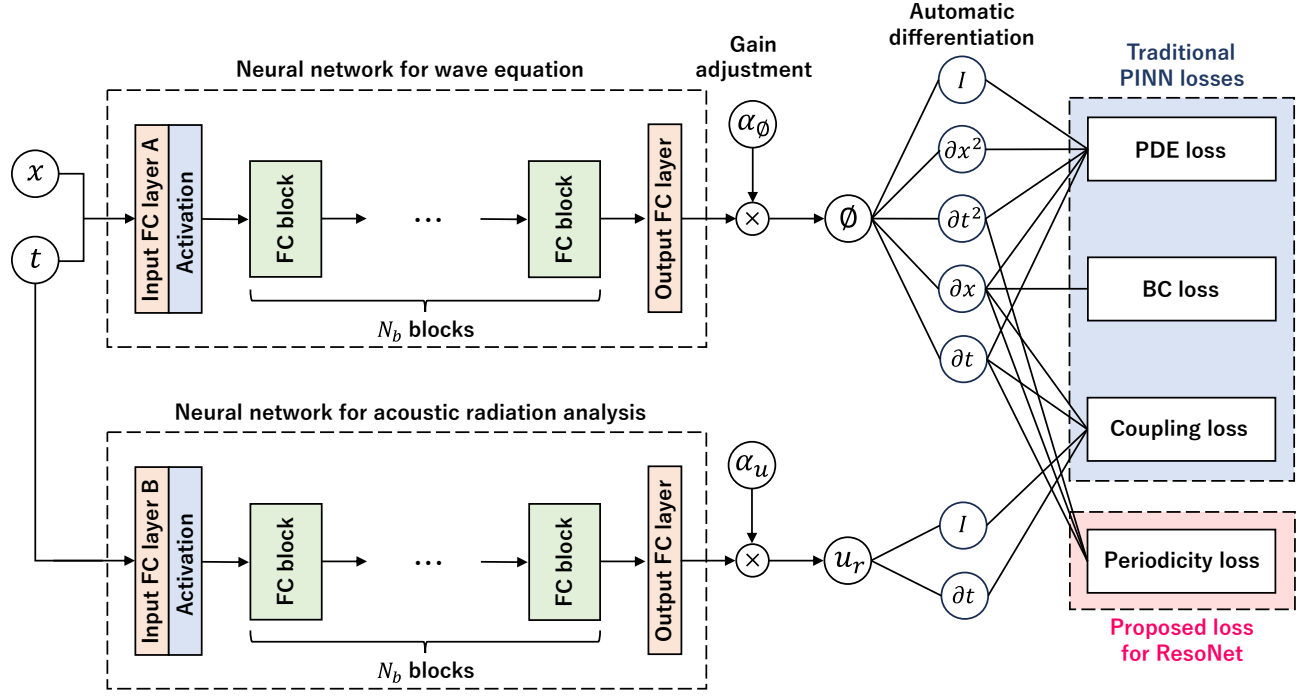


FIG. 3. (Color online) Structure of ResoNet. The upper neural network in the figure outputs the velocity potential ϕ , and the lower neural network outputs the volume velocity u_r with respect to the radiation. ϕ and u_r are input to coupling loss, and coupled analysis is performed. Periodicity Loss is the loss function proposed in this study, which forces u , p , and ϕ to be the same at $t = 0$ and $t = T$ (T : period).

of the external system (in this paper, acoustic radiation system). The vocal fold vibration system in speech production analysis and the spatial acoustic system in instrumental acoustics can be coupled with tube acoustics. Each PINN simulating the respective physical system has its suitable structure and scale (e.g., choice of activation function). Therefore, in this study, we separated the wave equation system and the acoustic radiation system into separate neural networks to facilitate modification of the neural network for the external system.

In this study, all activation functions used in the neural network shown in Fig. 3 are functions expressed as

$$f(a) = a + \sin^2 a, \quad (16)$$

where a denotes the input to the layer. This activation function, Snake, has been reported to be robust to periodic inputs⁴². Snake was selected as the activation function because of the better learning performance compared to the more traditional tanh and sin in preliminary simulations. Considerations regarding the choice of activation function are discussed in Appendix B.

We performed automatic differentiation on $\hat{\phi}_i$ and \hat{u}_{ri} , and the various loss functions shown on the right side of Fig. 3 are defined. The traditional PINN uses the PDE and boundary condition (BC) loss functions. The PDE loss introduces the constraints of Eq. (7), and the BC loss introduces constraints owing to the boundary conditions into the neural network. Coupling loss is

a type of PDE loss in traditional PINN, which introduces constraints owing to the coupling of the wave equation and the external system (acoustic radiation in this study) into the neural network, which is a type of PDE loss for conventional PINNs. We used periodicity loss that introduced constraints owing to the resonance periodicity. The following sections describe each item in detail.

B. Neural network blocks

As shown in Fig. 3, ResoNet has two neural network blocks: one calculates the solution of the wave equation in Eq. (7), whereas the other calculates the solution for the acoustic radiation circuit in Fig. 2.

1. Neural network for wave equation

This network uses x_i and t_i as inputs and predicts the velocity potential $\hat{\phi}_i$ for the wave equation. Initially, two-channel data (x_i, t_i) are fed to “Input FC layer A,” which is a fully connected layer⁴³ that outputs N_f channel data as Fig. 3 shows. An activation layer is present immediately thereafter, and it is the snake described in Section III A.

After the first activation layer, data are fed into the “FC block.” All FC blocks in Fig. 3 have the same structure, and its details are shown in Fig. 4. The fully connected layer in Fig. 4 has N_f input channels and N_f

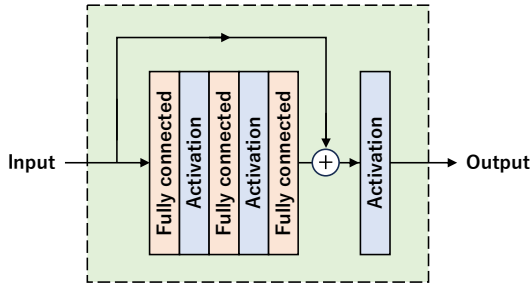


FIG. 4. (Color online) Details of FC block. There are two paths in the block, one calculated by fully connected layers and activation functions and the other by skip paths. All activation functions are 'snake'.

output channels, and the activation layer is the Snake, as shown in Eq. (16). To circumvent the vanishing gradient problem⁴⁴, a residual connection⁴⁵ is applied before the last activation layer.

After N_b FC blocks, we fed the data into the “Output FC layer,” a fully connected layer with N_f input channels and one output channel. The output value is multiplied by the gain adjustment parameter α_ϕ , and finally the neural network predicts the $\hat{\phi}_i$ value of the solution for the wave equation.

2. Neural network for acoustic radiation analysis

This network uses t_i as the input and predicts the \hat{u}_{ri} value of the equivalent circuit shown in Fig. 2. The only difference from the neural network for the wave equation (described in Section III B 1) is that the number of input channels is one (t_i only), and the “Input FC layer B” is a fully connected layer with one input channel and N_f output channels. All the other structures are identical to those described in Section III B 1.

C. Loss functions

The loss function of ResoNet is calculated as the sum of the following partial loss functions: traditional PINN losses (PDE loss, BC loss and Coupling loss), and periodicity loss.

1. Traditional PINN losses

As regards PDE loss, the output $\hat{\phi}_i$ of the neural network is defined as:

$$\hat{\phi}_{i,E} := F_w(x_i, t_i; \Theta_w), \quad x_i \in [0, l], \quad t_i \in [0, T], \quad (17)$$

where T is the simulation time (one resonance period in this study). For $\hat{\phi}_{i,E}$ to follow Eq. (7), the PDE loss is

defined as:

$$L_E = \frac{1}{N_E} \sum_{i=1}^{N_E} \left\{ \frac{\partial^2 \hat{\phi}_{i,E}}{\partial x_i^2} + \frac{1}{A_i} \frac{\partial A_i}{\partial x_i} \frac{\partial \hat{\phi}_{i,E}}{\partial x_i} - G_i R_i \hat{\phi}_{i,E} - \left(\frac{G_i \rho}{A_i} + \frac{R_i A_i}{K} \right) \frac{\partial \hat{\phi}_{i,E}}{\partial t_i} - \frac{\rho}{K} \frac{\partial^2 \hat{\phi}_{i,E}}{\partial t_i^2} \right\}^2, \quad (18)$$

where N_E is the number of collocation points for the PDE loss. The partial differential values of $\hat{\phi}_{i,E}$ are required to calculate Eqs. (18) are obtained via automatic differentiation⁴⁴ of the neural network.

Similarly, $\hat{\phi}_i$ must follow boundary conditions. As described in Section II B, the boundary condition in this study at $x = 0$ is given by the forced flow velocity. For the BC loss, the output $\hat{\phi}_i$ of the neural network is defined as:

$$\hat{\phi}_{i,B} := F_w(x_0, t_i; \Theta_w), \quad t_i \in [0, T], \quad (19)$$

where $x_0 = 0$. The loss function L_B with respect to the boundary condition is defined as:

$$L_B = \frac{1}{N_B} \sum_{i=1}^{N_B} (\hat{u}_{i,B} - \bar{u}_{i,B})^2, \quad (20)$$

where N_B is the number of collocation points for the BC loss and $\bar{u}_{i,B}$ is the volume flow velocity data given as the boundary condition. Based on Eq. (5), $\hat{u}_{i,B}$ is calculated from $\hat{\phi}_{i,B}$ using the following equation.

$$\hat{u}_i = -A_i \frac{\partial \hat{\phi}_i}{\partial x_i}. \quad (21)$$

2. Coupling loss (A type of PDE loss)

ResoNet incorporates the coupling condition between the system described by the wave equation and the external system as the coupling loss. Coupling loss is a type of PDE loss in traditional PINN. In this study, the external system is an acoustic radiation system, as shown in Fig. 2, and the Eqs. (10) and (11) describe coupling. In this section, we describe a method for calculating the coupling loss.

First, we define the output $\hat{\phi}_i$ of the neural network for the wave equation as:

$$\hat{\phi}_{i,C} := F_w(x_l, t_i; \Theta_w), \quad t_i \in [0, T], \quad (22)$$

where $x_l = l$. Based on Eq. (6), the sound pressure is obtained from $\hat{\phi}_i$ as follows.

$$\hat{p}_i = R_i A_i \hat{\phi}_i + \rho \frac{\partial \hat{\phi}_i}{\partial t_i}. \quad (23)$$

Let $\hat{u}_{i,C}$ and $\hat{p}_{i,C}$ be the volume velocity and sound pressure at $x = l$, obtained by applying Eqs. (21) and (23) to $\hat{\phi}_{i,C}$, respectively. Additionally, as defined in Eq. (15), let \hat{u}_{ri} be the output of the neural network for acoustic

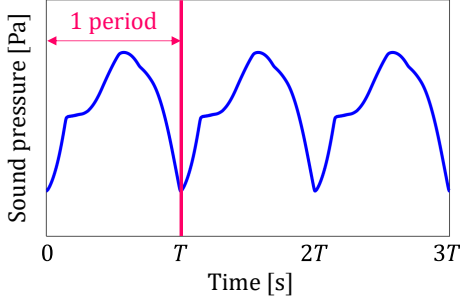


FIG. 5. (Color online) Sound pressure waveform at steady state of resonance. In the steady state of the resonance, the waveform changes little in each period.

radiation for input t_i . Based on Eqs. (10) and (11), the coupling loss L_C is defined as:

$$L_C = \frac{\lambda_l}{N_C} \sum_{i=1}^{N_C} \left\{ (\hat{u}_{ri} - \hat{u}_{i,C}) R_r - L_r \frac{d\hat{u}_{ri}}{dt_i} \right\}^2 + \frac{\lambda_r}{N_C} \sum_{i=1}^{N_C} \{ \hat{p}_{i,C} - (\hat{u}_{ri} - \hat{u}_{i,C}) R_r \}^2, \quad (24)$$

where N_C is the number of collocation points of the coupling loss; and λ_l and λ_r are the weight parameters of each term.

3. Periodicity loss

This section explains the core idea of ResoNet, the loss function with respect to periodicity. When performing time-domain resonance analysis, the transient state must be included until a steady state is reached. As mentioned in Section I, because sound waves have complex dynamics, a large-scale neural network is required to perform long simulations, which poses challenges in the computational cost and neural network convergence.

In the acoustic resonance analysis, the object of interest is one period in the steady state, as shown in Fig. 5. Therefore, in ResoNet, only one period was analyzed, and the function approximation capability of the neural network was effectively utilized. For this purpose, we formulated a “periodicity loss” function, which forces the output of the neural network to have the same value as $\hat{\phi}_i$ at $t = 0$ and $t = T$ in the steady state. The following describes the procedure for calculating periodicity loss.

First, the output $\hat{\phi}_i$ of the neural network for the wave equation is defined using the following two equations.

$$\begin{aligned} \hat{\phi}_{i,P1} &:= F_w(x_i, t_0; \Theta_w) \\ \hat{\phi}_{i,P2} &:= F_w(x_i, t_T; \Theta_w), \end{aligned} \quad x_i \in [0, l], \quad (25)$$

where $t_0 = 0$ and $t_T = T$ (T : period); and $\phi_{i,P1}$ and $\phi_{i,P2}$ are the values of the output $\hat{\phi}_i$ for times $t = 0$ and $t = T$ at the same position x_i , respectively.

The volume velocity is obtained from $\hat{\phi}_i$ using Eq. (21), and the sound pressure is obtained from $\hat{\phi}_i$ using Eq. (23). Let $\hat{u}_{i,P1}$ and $\hat{p}_{i,P1}$ be the volume velocity and sound pressure obtained from $\hat{\phi}_{i,P1}$, and let $\hat{u}_{i,P2}$ and $\hat{p}_{i,P2}$ be those obtained from $\hat{\phi}_{i,P2}$, respectively. In the steady state, if the input x_i (position) is the same, the continuity condition must hold between $\hat{p}_{i,P1}$ and $\hat{p}_{i,P2}$ and between $\hat{u}_{i,P1}$ and $\hat{u}_{i,P2}$. Therefore, the following loss functions are defined to force the neural network to enforce the conditions $\hat{p}_{i,P1} = \hat{p}_{i,P2}$ and $\hat{u}_{i,P1} = \hat{u}_{i,P2}$.

$$L_u = \frac{1}{N_P} \sum_{i=1}^{N_P} (\hat{u}_{i,P1} - \hat{u}_{i,P2})^2 \quad (26)$$

$$L_p = \frac{1}{N_P} \sum_{i=1}^{N_P} (\hat{p}_{i,P1} - \hat{p}_{i,P2})^2, \quad (27)$$

where N_P is the number of collocation points for the periodicity loss. Additionally, we define the following loss function to enforce the continuous condition of the time derivative.

$$L_t = \frac{1}{N_P} \sum_{i=1}^{N_P} \left(\frac{\partial^2 \hat{\phi}_{i,P1}}{\partial t_0^2} - \frac{\partial^2 \hat{\phi}_{i,P2}}{\partial t_T^2} \right)^2. \quad (28)$$

From Eqs. (26)–(28), the periodicity loss L_P proposed in this study is defined as

$$L_P = \lambda_u L_u + \lambda_p L_p + \lambda_t L_t, \quad (29)$$

where λ_u , λ_p and λ_t are the weight parameters for each term.

If the periodicity loss is not included, the proposed method can analyze non-periodic phenomena in a 1D acoustic tube with radiation at the open end.

4. Loss function for the whole network

The loss function L_{all} for the entire network was calculated as the sum of the traditional PINN losses, periodic loss, and coupling loss, as follows.

$$L_{all} = \lambda_E L_E + \lambda_B L_B + \lambda_P L_P + \lambda_C L_C, \quad (30)$$

where λ_E , λ_B , λ_P , and λ_C denote the weight parameters of the respective loss functions. Finally, we formulated the optimization problem of ResoNet as follows:

$$\min_{\Theta_w, \Theta_r} L_{all}(\Theta_w, \Theta_r). \quad (31)$$

By minimizing the loss function L_{all} , we optimized the trainable parameters Θ_w and Θ_r of the neural network. For this purpose, we used the Adam optimizer⁴⁶ to determine the optimal values of Θ_w and Θ_r through iterative calculations.

D. Implementation

We implemented ResoNet using the Deep Learning Toolbox in MATLAB (MathWorks, USA) and used the

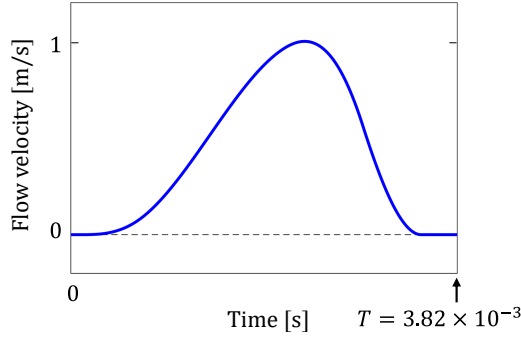


FIG. 6. (Color online) Forced flow velocity waveform (smoothed Rosenberg waveform). This waveform gives the boundary condition of the acoustic tube at $x = 0$.

“dlfeval” function to code a custom training loop. We used “sobolset” function from the Statistics and Machine Learning Toolbox to create datasets for x_i and t_i . The neural network was trained via GPU-assisted computation using the Parallel Computing Toolbox.

We performed the neural network training and prediction on a computer with a Core i9-13900KS CPU (Intel, USA) and GeForce RTX 4090 GPU (NVIDIA, USA) with 128 GB of main memory and 24 GB of video memory.

IV. VALIDATION OF PROPOSED METHOD

The performance of the proposed method was validated through forward and inverse analysis of the acoustic resonance using ResoNet.

A. Forward analysis

1. Analysis conditions for forward analysis

The effectiveness of the proposed method was assessed through a forward analysis of the acoustic tube, as shown in Fig. 1 using the boundary conditions described in Section II B. The length of the acoustic tube, l , was set to 1 m, and the diameter to 10 mm.

The forced-flow velocity waveform, given as a boundary condition, is a smoothed Rosenberg wave⁴⁷ as shown in Fig. 6. A moving average filter was applied to the original Rosenberg wave to smooth the waveform, similar to an R++ wave⁴⁸. The fundamental frequency F_0 of the forced flow waveform was 261.6 Hz (C4 on the musical scale). Therefore, $T = 3.82 \times 10^{-3}$ s.

The physical properties of air used in the analysis are listed in Table I. Ishizaka et al. calculated R by substituting a constant for ω_c in Eqs for the energy loss coefficients. (8)²⁷. In this study, we calculated R and G by substituting $\omega_c = 1643.7$ rad/s (261.6 Hz, C4 in the musical scale) in Eqs. (8) and (9), respectively; thus, we obtained $R = 6.99 \times 10^5$ m²/(Pa · s) and $G = 3.65 \times 10^{-7}$ Pa · s/m⁴.

TABLE I. Physical properties of air. The physical properties shown here are used in all forward and inverse analyses in this study.

Parameter	Value
Air density ρ	1.20 kg/m ³
Bulk modulus K	1.39×10^5 Pa
Speed of sound c	340 m/s
Viscosity coefficient μ	19.0×10^{-6} Pa · s
Heat capacity ratio η	1.40
Thermal conductivity λ	2.41×10^{-2} W/(m · K)
Specific heat for const. pressure c_p	1.01 kJ/(kg · K)

In the forward analysis, we set the number of nodes in the neural network N_f to 200 and the number of FC blocks N_b to five based on preliminary simulations. Further, we created a dataset (x_i, t_i) for each loss function, as follows. In Eq. (17) for the PDE loss calculation, we used quasi-random numbers generated by the “sobolset” function in MATLAB for x_i and t_i , and the number of collocation points N_E was 5000. Next, for t_i in Eq. (19), and Eq. (22) used in the calculation of the BC and coupling losses, the range $[0, T]$ was divided into 1000 equal parts to create a dataset of t_i ; thus, N_B and N_C were 1000. Finally, for x_i in Eqs. (25) used in calculating the periodicity loss, the range $[0, l]$ was divided into 1000 equal parts to create a dataset of x_i ; thus, N_P was 1000. The validity of the number of these collocation points is explained in Appendix C. As in Rasht-Behesht et al.²⁰, the value ranges of x_i and t_i were normalized to $[-1, 1]$ when inputting them into the neural network. The gain adjustment parameters were set to $\alpha_\phi = 0.002$ and $\alpha_u = 3.4 \times 10^{-5}$.

To compare the performance of the forward analysis, we used the finite difference method. The step size of the finite difference method was $\Delta x = 10^{-3}$ m, $\Delta t = 0.5 \times 10^{-6}$ s, and we used the CTCS (Centered-Time Centered-Space) scheme in the calculations. Appendix D describes the validity of the step size.

2. Hyperparameters of Neural Network

This section describes the PINN weight parameters and the learning rate of the Adam optimizer.

Setting appropriate weight parameters is critical for PINN learning. In this study, we determined the weight parameters by using a combination of two approaches: a normalization approach based on known boundary conditions and an empirical approach. First, for the known boundary condition at $x = 0$, the maximum particle velocity is 1 m/s, as shown in Fig. 6; therefore, the weight λ_B with respect to the boundary condition is normalized as follows

$$\lambda_B = \frac{\lambda'_B}{A_0^2} \quad (32)$$

where A_0 is the cross-sectional area at $x = 0$, and we set $\lambda'_B = 1$. With this λ'_B as a reference, the weight parameters λ_u , λ_l , and λ_t , which are related to the volume velocity, were normalized as follows.

$$\lambda_u = \frac{\lambda'_u}{A_0^2} \quad (33)$$

$$\lambda_l = \frac{\lambda'_l}{(R_r A_0)^2} \quad (34)$$

$$\lambda_r = \frac{\lambda'_r}{(R_r A_0)^2}, \quad (35)$$

Since the order of the particle velocity is nearly constant in the tube, λ'_B , λ'_u , λ'_l and λ'_r should have close orders. Finally, we empirically set $\lambda'_u = 1$, $\lambda'_l = 1$, and $\lambda'_r = 50$. The remaining λ_E , λ_p , and λ_t are weights with respect to pressure p and velocity potential ϕ . Therefore, we cannot infer the order from the boundary conditions. Hence, we empirically set them to $\lambda_E = 0.58$, $\lambda_p = 8.7 \times 10^{-6}$, and $\lambda_t = 1.3 \times 10^{-12}$. The final list of weight parameters used is shown in Table II.

TABLE II. Weight parameters for forward analysis. We determined these parameters by a combination of normalization and empirical approaches described in Section IV A 2.

Parameter	Value	Parameter	Value
λ_E	0.58	λ_r	1.4×10^{-4}
λ_B	1.6×10^8	λ_u	1.6×10^8
λ_P	1.0	λ_p	8.7×10^{-6}
λ_C	1.0	λ_t	1.3×10^{-12}
λ_l	2.9×10^{-6}		

We trained all collocation points as a single batch, and the learning rate of the Adam optimizer λ_{adam} was calculated by the following equation.

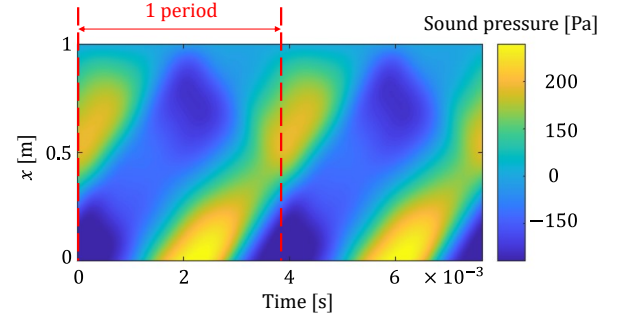
$$\lambda_{\text{adam}} = \frac{\lambda_{\text{init}}}{1 + \beta i_e} \quad (36)$$

where λ_{init} is the initial value of the learning rate, β is the decay coefficient, and i_e is the number of epochs. In this study, we set $\lambda_{\text{init}} = 0.001$ and $\beta = 0.007$ empirically.

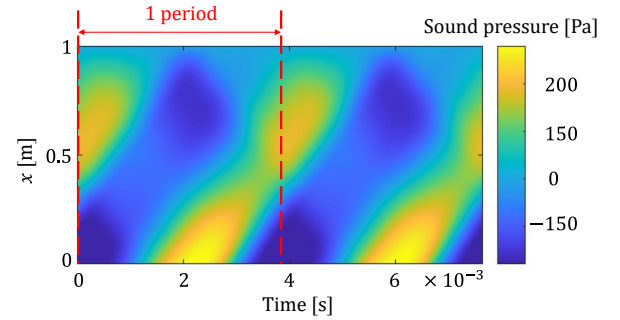
3. Results of forward analysis

Figure 7(a) shows the analyzed sound pressure in the range of $x = [0, l]$ and $t = [0, T]$ after 20,000 training epochs. Although we only analyzed one period, the same result is shown twice along the time axis to confirm the waveform continuity at $t = 0$ and $t = T$. The results of the finite difference method (FDM) are shown for comparison in Fig. 7(b). Figure 7 demonstrates strong agreement between the ResoNet and FDM analysis results. Figure 8 shows the differences between the results

of ResoNet and FDM. The difference was less than 1% in most regions; however, we noted some streaked regions with a difference of 2% or more. The regions with large differences are discussed later in this section.



(a) Result of ResoNet.



(b) Result of FDM.

FIG. 7. (Color online) Analyzed sound pressure. The results of the ResoNet forward analysis are in close agreement with the Finite Difference Method (FDM) analysis results.

Figure 9 shows the analyzed sound pressure waveforms at $x = l$, and Fig. 10 shows the frequency spectra. Although differences are observed in the high-frequency domain in Fig. 10, the ResoNet results in the time domain indicate its high accuracy in acoustic resonance analysis.

The regions with large differences in Fig. 8 were discussed considering the sound pressure waveform and frequency spectra. Figure 11 shows the difference and sound pressure waveforms for one period on the same timescale; evidently, the difference is huge in region A. The corresponding region in the sound pressure waveform shows a difference between the FDM and ResoNet waveforms at the points indicated by B and C. At point B, the waveform suddenly changes from monotonically decreasing to monotonically increasing, and at point C, it shifts from monotonically increasing to a horizontal phase. Considering that a neural network is a function approximator, such steep waveform changes may not have been approximated well by ResoNet. This is evident from the difference between FDM and ResoNet in

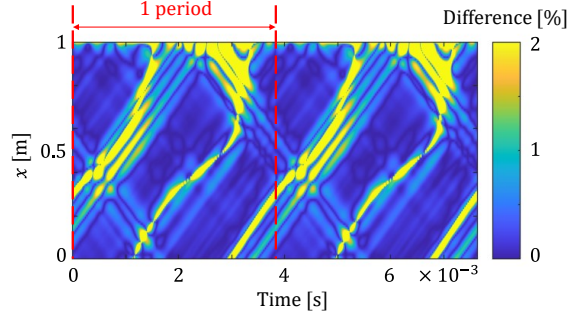


FIG. 8. (Color online) Difference of the ResoNet from the FDM. In most regions, the difference is less than 1%, but there are some regions where the difference is greater than 1%. The regions with large differences are discussed in Fig. 11.

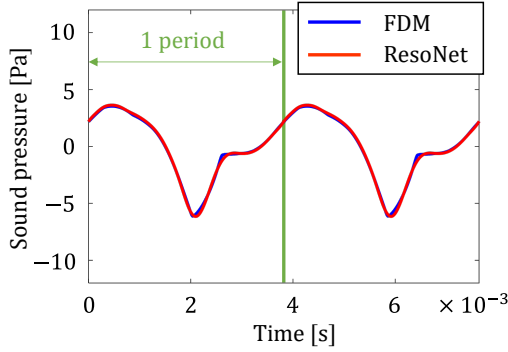


FIG. 9. (Color online) Sound pressure waveforms at $x = l$. The forward analysis by the proposed method is in good agreement with the results of the finite difference method (FDM), but there are some differences. These differences are discussed in Fig. 11.

the high-frequency region shown in Fig. 10. Thus, like other PINNs, ResoNet accurately analyzes in the low-frequency domain; however, its accuracy degrades in the high-frequency domain due to a problem known as the F-principle⁴⁹. Introducing Fourier Features⁵¹ could improve the approximation ability of PINNs at high frequencies, addressing this issue. The problem of reduced approximation accuracy at high frequencies could be improved by modifying the structure of the neural network and learning method, which remain a subject for future studies.

To confirm the state of convergence, Fig. 12 shows the loss function for each epoch. Figure 12 shows the total L_{all} and each loss term separately. Since we had confirmed through preliminary simulations that PINN learning stabilizes and generally converges when L_{all} falls below 10^{-5} , we stopped learning at 20,000 epochs, which fulfills this condition this time.

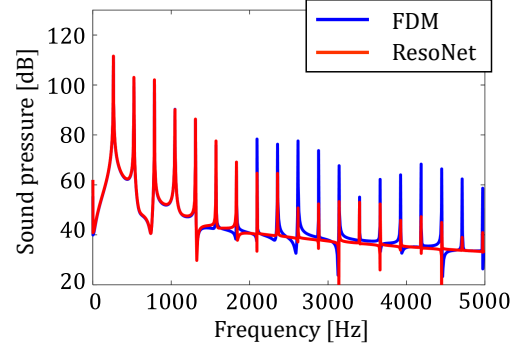


FIG. 10. (Color online) Frequency spectra of the waveforms of Fig. 9. The proposed method and FDM agree well up to approximately 2000 Hz, but the differences are larger at higher frequencies. This decrease in neural network approximation accuracy at high frequencies is called F-principle⁴⁹. Fourier features⁵⁰ have been proposed as a method to improve the approximation performance at high frequencies, and applying Fourier features in ResoNet is a subject for future study.

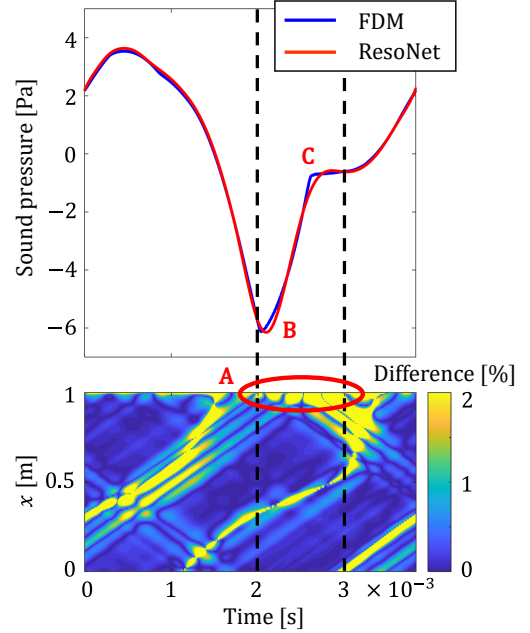


FIG. 11. (Color online) Sound pressure waveforms at $x = l$ and errors in the same time scale. Due to the F-principle of neural networks⁴⁹, the proposed method does not approximate well the part where the waveform changes steeply. This difference in waveforms leads to the difference in the high-frequency range shown in Fig. 10.

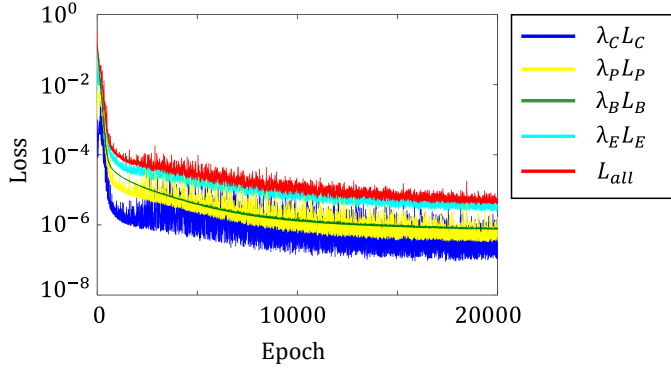


FIG. 12. (Color online) Losses per epoch. The figure is plotted separately for each loss function. Sufficient convergence is obtained at 20,000 epochs.

B. Inverse analysis

Additionally, we performed an inverse analysis on the acoustic tube, as shown in Fig. 1, using the boundary conditions in Section II B. The forced-flow waveform and physical properties were identical to those described in Section IV A 1.

We considered two specific situations for inverse analysis: first, the identification of energy loss coefficients, and second, the design optimization of acoustic tubes. The information provided to ResoNet has two waveforms: a flow waveform at $x = 0$ and a sound pressure waveform at $x = L$.

1. Additional loss function for inverse analysis

The loss function for the sound pressure waveform at $x = l$ was introduced into ResoNet using the following procedure: First, the output $\hat{\phi}_{i,M}$ is defined as:

$$\hat{\phi}_{i,M} := F_w(x_l, t_i; \Theta_w), \quad t_i \in [0, T], \quad (37)$$

where $x_l = l$. The loss function for the sound pressure at $x = l$ is defined as:

$$L_M = \frac{1}{N_M} \sum_{i=1}^{N_M} (\hat{p}_{i,M} - \bar{p}_{i,M})^2, \quad (38)$$

where N_M denotes the number of collocation points for the loss. $\hat{p}_{i,M}$ was obtained from $\hat{\phi}_{i,M}$ by using Eq. (23) and $\bar{p}_{i,M}$, the measured sound pressure waveform, was obtained from the analysis results of FDM simulation. Fig. 12 shows the waveform. The loss function for the entire network is defined as:

$$L_{all} = \lambda_E L_E + \lambda_B L_B + \lambda_P L_P + \lambda_C L_C + \lambda_M L_M, \quad (39)$$

where λ_M is the weight parameter of L_M .

In the inverse analysis, we set the number of nodes in the neural network N_f to 400 and the number of FC blocks N_b to two based on preliminary simulations. We

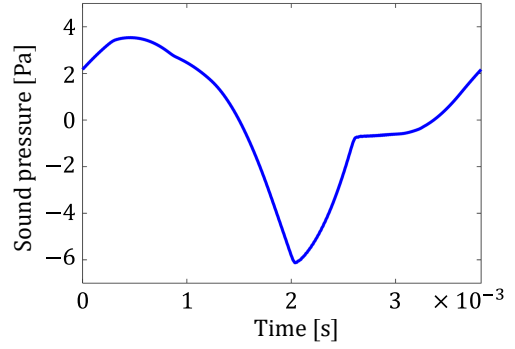


FIG. 13. (Color online) Sound pressure waveform at $x = l$ (obtained by FDM simulation). This waveform is given to the new loss function L_M as a boundary condition that the neural network's output must satisfy during the inverse analysis.

determined the order of the weight parameters of the loss function in the same way as described in Section IV A 2, and the parameters used in the inverse analysis are shown in Table III. We set the initial value of the learning rate of the Adam optimizer to $\lambda_{init} = 0.001$ and the decay coefficient to $\beta = 0.005$.

TABLE III. Weight parameters for inverse analysis. We determined these parameters by combining normalization and empirical approaches as in the forward analysis.

Parameter	Value	Parameter	Value
λ_E	5.8	λ_r	1.4×10^{-4}
λ_B	1.6×10^8	λ_u	1.6×10^8
λ_P	1.0	λ_p	8.7×10^{-6}
λ_C	1.0	λ_t	1.3×10^{-12}
λ_l	2.9×10^{-6}	λ_M	5.0×10^{-3}

2. Case 1: Identification of energy loss coefficients

Assuming that the energy-loss coefficients follow Eqs. (8)–(9) and ω_c in these equations is unknown, we performed an inverse analysis to determine ω_c . As described at the beginning of section IV B, the flow velocity waveform at $x = 0$ (Fig. 6) and the sound pressure waveform at position $x = l$ (Fig. 13) are given to ResoNet. Because w_c is a trainable parameter of the neural network, we formulated the optimization problem as follows:

$$\min_{\Theta_w, \Theta_r, \omega_c} L_{all}(\Theta_w, \Theta_r, \omega_c). \quad (40)$$

Fig. 14 shows the identification results. We set the initial value of ω_c to 1.3149×10^3 (20% error) for a true value of 1.6437×10^3 ; however, after 100,000 training epochs, the

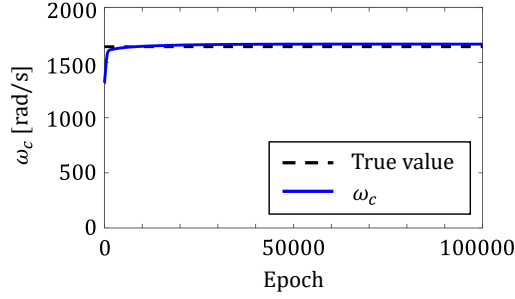


FIG. 14. (Color online) Identification result of ω_c . An error of 20% was given as the initial value of ω_c , but the error of ω_c after 100,000 epochs of training dropped to 1.01%.

value converged to 1.6671×10^3 , which indicated that ω_c could be identified with an error of 1.01%.

For reference, we also performed the inverse analysis by mixing 1% uncorrelated Gaussian noise into \bar{u}_B and \bar{p}_M given as training data. ω_c after 100,000 epochs of training was 1678.2 (1.02% error), indicating that the inverse analysis can be performed as well as the noiseless case if the noise is approximately 1%.

3. Case 2: Design optimization of acoustic tube

This section describes the design optimization of the length l and diameter d of the acoustic tube that simultaneously satisfies the flow velocity waveform at $x = 0$ and the sound pressure waveform at $x = l$. The flow velocity waveform at $x = 0$ in Fig. 6 and the sound pressure waveform at $x = l$ in Fig. 12 were given to ResoNet. Because l and d are the trainable parameters of the neural network, the optimization problem was formulated as:

$$\min_{\Theta_w, \Theta_r, l, d} L_{all}(\Theta_w, \Theta_r, l, d). \quad (41)$$

The number of collocation points does not change during the calculation, even when encountering variable length. The relative positions of the collocation points at $0 \leq x \leq l$ also do not change during the calculation. We introduced a length-adjusting factor while calculating the partial derivative when handling variable length. Let the initial length of the tube be l_0 , and the tube length as a variable be l_v . The following equation obtains the spatial derivative of ϕ at $l = l_v$.

$$\left(\frac{\partial \phi}{\partial x} \right)_{l=l_v} = \frac{l_0}{l_v} \left(\frac{\partial \phi}{\partial x} \right)_{l=l_0}. \quad (42)$$

The $\partial \phi / \partial x$ at initial length $l = l_0$ can be obtained by automatic differentiation, and by substituting Eq. (42) into the partial differential equation when calculating the loss function, it is possible to calculate the loss at $l = l_v$.

Fig. 15 shows the identification results. We set the initial value of l to 0.8 (20% error) for an optimal value of 1 and the initial value of d to 8 (20% error) for an optimal value of 10. Table IV indicates that l and d were identified with high accuracy with respect to the optimal values

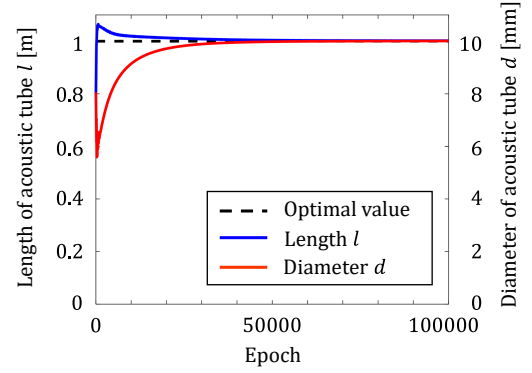


FIG. 15. (Color online) Identification result of l and d . A 20% error was given as the initial value of l and d , but after 100,000 training epochs, they converged to a value close to the optimal value.

after 100,000 training epochs. Table IV also shows the results when 1% uncorrelated Gaussian noise was mixed into the training data \bar{u}_B and \bar{p}_M for reference, indicating that the inverse analysis can be performed with the same level of accuracy as the noiseless case.

TABLE IV. Optimal and identified value of l and d . An error of 20% was given as the initial value, but after 100,000 epochs of training, the error was significantly reduced.

	Length l [m]	Diameter d [mm]
Optimal	1	10
Identified (no noise)	1.0022 (0.22% error)	10.009 (0.09% error)
Identified (1% noise)	1.0024 (0.24% error)	10.004 (0.04% error)

V. CONCLUSION

In this study, we proposed ResoNet, a PINN for analyzing acoustic resonance, and demonstrated its effectiveness by performing a time-domain analysis of acoustic resonance by introducing a loss function for periodicity into a neural network.

The forward analysis performed using an acoustic tube of 1 m, the scale of a musical instrument or car muffler, revealed that acoustic resonance analysis could be performed with sufficient accuracy in the time domain. The accuracy of the analysis decreased with abrupt changes in the sound pressure waveform and the high-frequency region in the frequency domain. Given that this is due to the function approximation capability of the neural network, designing a PINN structure that

is more suitable for acoustic analysis is a topic for future studies.

We identified the energy loss coefficient in the acoustic tube for the inverse analysis and optimized its design. In these inverse problems, the true and optimal values could be identified with high accuracy from the waveform data at the endpoints of the acoustic tube.

These results indicate that PINN may be a new option for acoustic inverse problems. This highlights the potential for broad applicability for parameter identification and other inverse problems related to 1D acoustic tubes, such as the design optimization of musical instruments and glottal inverse filtering (GIF). In future work, we intend to address these acoustic inverse problems using ResoNet.

ACKNOWLEDGMENTS

JSPS KAKENHI Grant Number JP22K14447 supported this work.

AUTHOR DECLARATIONS

Conflict of Interest

The authors have no conflicts to disclose.

DATA AVAILABILITY

The data that support the findings of this study are available within the article.

APPENDIX A: DERIVATION OF WAVE EQUATION

This section describes the derivation of the wave equation using the energy-loss terms (Eq. (7)). First, the telegrapher's equation in the time domain (Eq. (3) and (4)).

$$\frac{\partial u}{\partial x} = -Gp - \frac{A}{K} \frac{\partial p}{\partial t}, \quad (\text{A1})$$

$$\frac{\partial p}{\partial x} = -Ru - \frac{\rho}{A} \frac{\partial u}{\partial t}. \quad (\text{A2})$$

The velocity potential is defined as:

$$u = -A \frac{\partial \phi}{\partial x}. \quad (\text{A3})$$

By substituting Eq. (A3) into Eq. (A2), we obtain:

$$p = RA\phi + \rho \frac{\partial \phi}{\partial t}. \quad (\text{A4})$$

By substituting Eqs. (A3) and (A4) into Eq. (A1), we obtain:

$$\begin{aligned} -\frac{\partial}{\partial x} \left(A \frac{\partial \phi}{\partial x} \right) &= -G \left(RA\phi + \rho \frac{\partial \phi}{\partial t} \right) \\ &\quad - \frac{A}{K} \frac{\partial}{\partial t} \left(RA\phi + \rho \frac{\partial \phi}{\partial t} \right). \end{aligned} \quad (\text{A5})$$

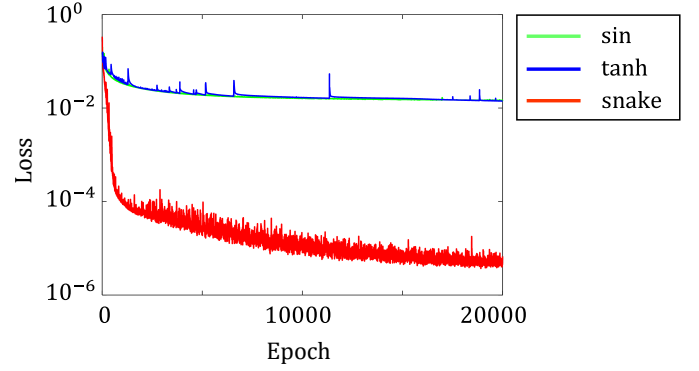


FIG. 16. (Color online) Comparison of losses for different activation functions. Compared to sin and tanh, snake shows very high convergence performance. The exact reason for this difference in convergence performance is unclear, but snake has a linear term in addition to the periodic nonlinear term, which may have affected the difference in convergence performance.

We obtain the following wave equation with energy loss terms by expanding and simplifying Eq. (A5).

$$\frac{\partial^2 \phi}{\partial x^2} + \frac{1}{A} \frac{\partial A}{\partial x} \frac{\partial \phi}{\partial x} = GR\phi + \left(\frac{G\rho}{A} + \frac{RA}{K} \right) \frac{\partial \phi}{\partial t} + \frac{\rho}{K} \frac{\partial^2 \phi}{\partial t^2}. \quad (\text{A6})$$

APPENDIX B: ACTIVATION FUNCTION

This section describes ResoNet's choice of activation function. The reason for using snake as the activation function is the better learning performance compared to the more common tanh and sin in preliminary simulations. Figure 16 shows the losses when forward analysis uses tanh, sin, or snake as the activation function. From the figure, the highest performance is achieved when snake is used as the activation function.

The reason why snake shows the highest performance is not exactly clear. However, some insight can be obtained from the snake equation. The following is a restatement of the snake's equation in the paper.

$$f(a) = a + \sin^2 a, \quad (\text{B1})$$

From Eq. (B1), snake has a linear term in the first term and a periodic $\sin^2 a$ in the second term. A periodic activation function such as sin can be regarded as a representation of the signal using the Fourier series^{24,52}. In the second term, snake with periodic $\sin^2 a$ effectively approximates periodic functions⁴². For these reasons, snake may have been suitable for the periodic resonance state sound waves treated in this study.

Also, unlike sin, snake has a linear term in the first term. Therefore, the vanishing gradient problem is mitigated by using snake compared to tanh and sin, and the

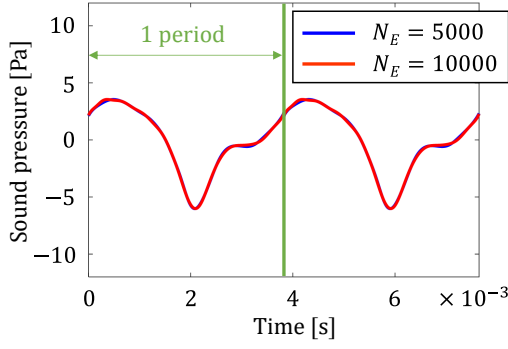


FIG. 17. (Color online) Sound pressure waveforms at $x = l$ analyzed by ResoNet for different number of collocation points N_E . There is little difference between the cases of 5,000 and 10,000 collocation points.

learning process could have been more effective at deeper layers by using snake.

APPENDIX C: COLLOCATION POINTS

This section describes the validity of the number of collocation points. In the forward analysis, The number of collocation points N_E of the PDE loss is 5000, and the average number of divisions along the time axis is 70.7. Considering that the period of the Rosenberg wave used in this study is 3.82×10^{-3} s, this number of divisions corresponds to a sampling frequency of 18.5 kHz. Since the fundamental frequency of the Rosenberg wave is 261.6 Hz, the time resolution of the N_E is sufficient considering the Nyquist theorem. The average number of spatial divisions is similarly 70.7, corresponding to $\Delta x = 0.014$ m when the acoustic tube length $l = 1$ m is considered. Assuming that the frequency under analysis is the highest 5000 Hz, the number of sampling points per wavelength ppw at 5000 Hz is

$$ppw = \frac{c}{5000\Delta x} = 4.81 \quad (C1)$$

which satisfies the Nyquist theorem.

The number of collocation points N_B and N_C for BC loss and coupling loss is 1000 in the time direction, which is sufficient from the above discussion. The number of collocation points N_P for Periodicity loss is 1000 in the spatial direction, which is also sufficient from the above discussion.

For reference, Fig. 17 compares the case with N_E of 5000 (the number of collocation points adopted in this study) and the case with 10000 and shows that the analysis results with N_E of 5000 are almost similar to those with 10000.

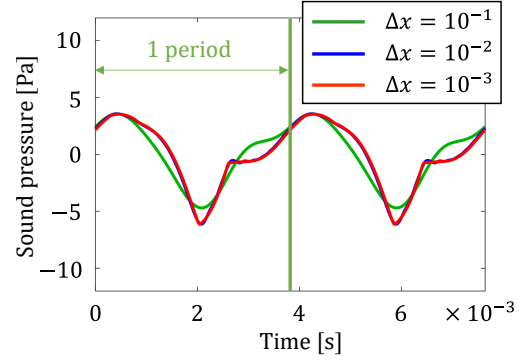


FIG. 18. (Color online) Sound pressure waveforms at $x = l$ analyzed by finite difference method for different spatial resolutions. Since there is little difference in spatial resolution between the $\Delta x = 10^{-2}$ and $\Delta x = 10^{-3}$ cases, the $\Delta x = 10^{-3}$ used in this study has sufficient resolution.

APPENDIX D: STEP SIZE FOR FDM

In this section, we describe the step size of the finite difference method. The time step size of $\Delta t = 0.5 \times 10^{-6}$ s corresponds to a resolution of 2×10^6 Hz, which is sufficient considering that the fundamental frequency of the Rosenberg wave analyzed in this study is 261.6 Hz. For the spatial resolution, a comparison of $\Delta x = 10^{-1}$, 10^{-2} , and 10^{-3} m is shown in Fig. 18. $\Delta x = 10^{-2}$ and 10^{-3} are almost similar, indicating that $\Delta x = 10^{-3}$ is sufficient for the required resolution.

APPENDIX E: INITIAL CONDITIONS

In this section, we investigate the effect of initial conditions on the inverse analysis. We performed the inverse analysis using the training data, shifted by $T/2$ (T : period) from the original \bar{u}_B and \bar{p}_M .

The results of the inverse analysis are shown in Table V and VI. Table A shows the result of the identification of ω_c (Section IVB2), and Table A shows the result of design optimization (Section IVB3). Table V and VI show that, although there are some differences in accuracy, the inverse analysis can be performed with accuracy close to that of the original conditions, even when the data given as initial conditions are different.

¹A. v. d. Oord, S. Dieleman, H. Zen, K. Simonyan, O. Vinyals, A. Graves, N. Kalchbrenner, A. Senior, and K. Kavukcuoglu, “Wavenet: A generative model for raw audio,” arXiv:1609.03499 (2016).

²I. Elias, H. Zen, J. Shen, Y. Zhang, Y. Jia, R. Skerry-Ryan, and Y. Wu, “Parallel Tacotron 2: A Non-Autoregressive Neural TTS Model with Differentiable Duration Modeling,” in *Proc. Interspeech 2021* (2021), pp. 141–145.

³A. Krizhevsky, I. Sutskever, and G. E. Hinton, “Imagenet classification with deep convolutional neural networks,” in *Advances in Neural Information Processing Systems* (2012), Vol. 25.

TABLE V. Optimal and identified value of ω_c . Even with different initial conditions, the proposed method can perform the inverse analysis with comparable accuracy.

	ω_c [rad/s]
Optimal	1643.7
Identified (original)	1667.1 (1.01% error)
Identified ($T/2$ shifted)	1660.4 (1.01% error)

TABLE VI. Optimal and identified value of l and d . Even with different initial conditions, the proposed method can perform the inverse analysis with comparable accuracy.

	Length l [m]	Diameter d [mm]
Optimal	1	10
Identified (original)	1.0022 (0.22% error)	10.009 (0.09% error)
Identified ($T/2$ shifted)	1.0031 (0.31% error)	9.8610 (1.39% error)

⁴F. N. Iandola, S. Han, M. W. Moskewicz, K. Ashraf, W. J. Dally, and K. Keutzer, "Squeezenet: Alexnet-level accuracy with 50x fewer parameters and 0.5 mb model size," arXiv:1602.07360 (2016).

⁵J. Ling, A. Kurawski, and J. Templeton, "Reynolds averaged turbulence modelling using deep neural networks with embedded invariance," *Journal of Fluid Mechanics* **807**, 155–166 (2016).

⁶R. Fang, D. Sondak, P. Protopapas, and S. Succi, "Neural network models for the anisotropic reynolds stress tensor in turbulent channel flow," *Journal of Turbulence* **21**(9-10), 525–543 (2020).

⁷K. Guo, Z. Yang, C.-H. Yu, and M. J. Buehler, "Artificial intelligence and machine learning in design of mechanical materials," *Materials Horizons* **8**(4), 1153–1172 (2021).

⁸D. Kochkov, J. A. Smith, A. Alieva, Q. Wang, M. P. Brenner, and S. Hoyer, "Machine learning-accelerated computational fluid dynamics," *Proceedings of the National Academy of Sciences* **118**(21), e2101784118 (2021).

⁹B. Kim, V. C. Azevedo, N. Thuerey, T. Kim, M. Gross, and B. Solenthaler, "Deep fluids: A generative network for parameterized fluid simulations," in *Computer graphics forum* (2019), Vol. 38, pp. 59–70.

¹⁰M. Raissi, P. Perdikaris, and G. E. Karniadakis, "Physics-informed neural networks: A deep learning framework for solving forward and inverse problems involving nonlinear partial differential equations," *Journal of Computational physics* **378**, 686–707 (2019).

¹¹L. B. Rall, *Automatic differentiation: Techniques and applications* (Springer, 1981).

¹²Z. Mao, A. D. Jagtap, and G. E. Karniadakis, "Physics-informed neural networks for high-speed flows," *Computer Methods in Applied Mechanics and Engineering* **360**, 112789 (2020).

¹³A. D. Jagtap, Z. Mao, N. Adams, and G. E. Karniadakis, "Physics-informed neural networks for inverse problems in supersonic flows," *Journal of Computational Physics* **466**, 111402 (2022).

¹⁴S. Cai, Z. Wang, S. Wang, P. Perdikaris, and G. E. Karniadakis, "Physics-informed neural networks for heat transfer problems," *Journal of Heat Transfer* **143**(6), 060801 (2021).

¹⁵H. Igel, *Computational Seismology: A Practical Introduction* (Oxford University Press, 2016).

¹⁶B. Moseley, A. Markham, and T. Nissen-Meyer, "Solving the wave equation with physics-informed deep learning," arXiv preprint arXiv:2006.11894 (2020).

¹⁷S. Alkhadhr, X. Liu, and M. Almekkawy, "Modeling of the forward wave propagation using physics-informed neural networks," in *2021 IEEE International Ultrasonics Symposium (IUS)* (2021), pp. 1–4.

¹⁸H. Wang, J. Li, L. Wang, L. Liang, Z. Zeng, and Y. Liu, "On acoustic fields of complex scatterers based on physics-informed neural networks," *Ultrasonics* **128**, 106872 (2023).

¹⁹S. Karimpouli and P. Tahmasebi, "Physics informed machine learning: Seismic wave equation," *Geoscience Frontiers* **11**(6), 1993–2001 (2020).

²⁰M. Rasht-Behesht, C. Huber, K. Shukla, and G. E. Karniadakis, "Physics-informed neural networks (pinns) for wave propagation and full waveform inversions," *Journal of Geophysical Research: Solid Earth* **127**(5), e2021JB023120 (2022).

²¹Y. Zhang, X. Zhu, and J. Gao, "Seismic inversion based on acoustic wave equations using physics-informed neural network," *IEEE transactions on geoscience and remote sensing* **61**, 1–11 (2023).

²²M. Olivieri, M. Pezzoli, F. Antonacci, and A. Sarti, "A physics-informed neural network approach for nearfield acoustic holography," *Sensors* **21**(23), 7834 (2021).

²³H. Kafri, M. Olivieri, F. Antonacci, M. Moradi, A. Sarti, and S. Gannot, "Grad-cam-inspired interpretation of nearfield acoustic holography using physics-informed explainable neural network," in *ICASSP 2023-2023 IEEE International Conference on Acoustics, Speech and Signal Processing (ICASSP)* (2023), pp. 1–5.

²⁴N. Borrel-Jensen, A. P. Engsig-Karup, and C.-H. Jeong, "Physics-informed neural networks for one-dimensional sound field predictions with parameterized sources and impedance boundaries," *JASA Express Letters* **1**(12) (2021).

²⁵N. Borrel-Jensen, S. Goswami, A. P. Engsig-Karup, G. E. Karniadakis, and C.-H. Jeong, "Sound propagation in realistic interactive 3d scenes with parameterized sources using deep neural operators," *Proceedings of the National Academy of Sciences* **121**(2) (2024).

²⁶L. Lu, P. Jin, and G. E. Karniadakis, "Deeponet: Learning nonlinear operators for identifying differential equations based on the universal approximation theorem of operators," arXiv preprint arXiv:1910.03193 (2019).

²⁷K. Ishizaka and J. L. Flanagan, "Synthesis of voiced sounds from a two-mass model of the vocal cords," *Bell system technical journal* **51**(6), 1233–1268 (1972).

²⁸L. Cveticanin *et al.*, "Review on mathematical and mechanical models of the vocal cord," *Journal of Applied Mathematics* **2012** (2012).

²⁹B. H. Story and I. R. Titze, "Voice simulation with a body-cover model of the vocal folds," *The Journal of the Acoustical Society of America* **97**(2), 1249–1260 (1995).

³⁰L. P. Fulcher and R. C. Scherer, "Recent measurements with a synthetic two-layer model of the vocal folds and extension of titze's surface wave model to a body-cover model," *The Journal of the Acoustical Society of America* **146**(6), EL502–EL508 (2019).

³¹S. Adachi and M.-a. Sato, "Time-domain simulation of sound production in the brass instrument," *The Journal of the Acoustical Society of America* **97**(6), 3850–3861 (1995).

³²J.-F. Petiot, R. Tournemene, and J. Gilbert, "Physical modeling sound simulations for the study of the quality of wind instruments," in *ICSV2019-26th International Congress on Sound and Vibration* (2019).

- ³³E. Ducasse, "A physical model of a single-reed wind instrument including actions of the player," *Computer Music Journal* **27**(1), 59–70 (2003).
- ³⁴V. Chatziioannou and M. van Walstijn, "Reed vibration modelling for woodwind instruments using a two-dimensional finite difference method approach," in *International Symposium on Musical Acoustics* (2007).
- ³⁵K. Yokota, S. Ishikawa, K. Takezaki, Y. Koba, and S. Kijimoto, "Numerical analysis and physical consideration of vocal fold vibration by modal analysis," *Journal of Sound and Vibration* **514** (2021).
- ³⁶M. Rothenberg, "A new inverse-filtering technique for deriving the glottal air flow waveform during voicing," *The Journal of the Acoustical Society of America* **53**(6) (1973).
- ³⁷J. Dang and K. Honda, "Estimation of vocal tract shapes from speech sounds with a physiological articulatory model," *Journal of Phonetics* **30**(3) (2002).
- ³⁸K. Hornik, M. Stinchcombe, and H. White, "Multilayer feedforward networks are universal approximators," *Neural networks* **2**(5), 359–366 (1989).
- ³⁹J. L. Flanagan, *Speech analysis synthesis and perception*, Vol. 3 (Springer Science & Business Media, 2013).
- ⁴⁰K. Yokota, S. Ishikawa, Y. Koba, S. Kijimoto, and S. Sugiki, "Inverse analysis of vocal sound source using an analytical model of the vocal tract," *Applied Acoustics* **150**, 89–103 (2019).
- ⁴¹T. H  lie, T. H  zard, R. Mignot, and D. Matignon, "One-dimensional acoustic models of horns and comparison with measurements," *Acta acustica united with Acustica* **99**(6), 960–974 (2013).
- ⁴²L. Ziyin, T. Hartwig, and M. Ueda, "Neural networks fail to learn periodic functions and how to fix it," *Advances in Neural Information Processing Systems* **33**, 1583–1594 (2020).
- ⁴³B. Kr  se, B. Krose, P. van der Smagt, and P. Smagt, "An introduction to neural networks," *J Comput Sci* **48** (1993).
- ⁴⁴J. Schmidhuber, "Deep learning in neural networks: An overview," *Neural networks* **61** (2015).
- ⁴⁵K. He, X. Zhang, S. Ren, and J. Sun, "Deep residual learning for image recognition," in *Proceedings of the IEEE conference on computer vision and pattern recognition* (2016).
- ⁴⁶D. P. Kingma and J. Ba, "Adam: A method for stochastic optimization," *arXiv preprint arXiv:1412.6980* (2014).
- ⁴⁷A. E. Rosenberg, "Effect of glottal pulse shape on the quality of natural vowels," *The Journal of the Acoustical Society of America* **49**(2B) (1971).
- ⁴⁸R. Veldhuis, "A computationally efficient alternative for the liljencrants-fant model and its perceptual evaluation," *The Journal of the Acoustical Society of America* **103**(1) (1998).
- ⁴⁹Z.-Q. J. Xu, Y. Zhang, T. Luo, Y. Xiao, and Z. Ma, "Frequency principle: Fourier analysis sheds light on deep neural networks," *arXiv preprint arXiv:1901.06523* (2019).
- ⁵⁰M. Tancik, P. Srinivasan, B. Mildenhall, S. Fridovich-Keil, N. Raghavan, U. Singhal, R. Ramamoorthi, J. Barron, and R. Ng, "Fourier features let networks learn high frequency functions in low dimensional domains," *Advances in neural information processing systems* **33** (2020).
- ⁵¹C. Song and Y. Wang, "Simulating seismic multifrequency wavefields with the fourier feature physics-informed neural network," *Geophysical Journal International* **232**(3) (2023).
- ⁵²N. Benbarka, T. H  fer, A. Zell, *et al.*, "Seeing implicit neural representations as fourier series," in *Proceedings of the IEEE/CVF Winter Conference on Applications of Computer Vision* (2022).